

# Long-range angular correlations on the near and away side in p–Pb collisions at $\sqrt{s_{\text{NN}}} = 5.02$ TeV

J.F. Grosse-Oetringhaus, A. Morsch, C. Loizides, T. Schuster

April 3, 2013

**Revision: 790**

## Contents

<b>1</b>	<b>Datasets</b>	<b>2</b>
<b>2</b>	<b>Event Selection</b>	<b>2</b>
<b>3</b>	<b>Track Selection</b>	<b>3</b>
<b>4</b>	<b>Event Classes</b>	<b>3</b>
<b>5</b>	<b>Correlation Function</b>	<b>4</b>
<b>6</b>	<b>Comparison with Alternative Averaging Procedures</b>	<b>6</b>
<b>7</b>	<b>Corrections</b>	<b>7</b>
7.1	MC Closure Test . . . . .	7
<b>8</b>	<b>Subtraction Procedure</b>	<b>12</b>
8.1	Subtraction Procedure with pp Collisions . . . . .	12
<b>9</b>	<b><math>v_n</math> Extraction</b>	<b>21</b>
<b>10</b>	<b>Yield Extraction</b>	<b>21</b>
<b>11</b>	<b>Width</b>	<b>21</b>
<b>12</b>	<b>Systematic Uncertainties</b>	<b>23</b>
12.1	Track Cuts . . . . .	23
12.2	MC Generator and Corrections . . . . .	23
12.3	Baseline Evaluation . . . . .	23
12.4	Residual Near-Side Peak . . . . .	23
12.5	Effect of Systematic Uncertainties . . . . .	24
12.6	Summary . . . . .	29
<b>13</b>	<b>Mirroring Procedure</b>	<b>30</b>
13.1	Method Comparison . . . . .	32

This analysis note discusses the details of the analysis done for the paper published as arXiv:1212.2001. In this paper two-particle correlations are presented in p–Pb collisions and by calculating the difference of the correlation in high-multiplicity and low-multiplicity events a  $\cos 2\Delta\varphi$  structure (“double ridge”) is revealed which has not been observed before. Many analysis details are the same as in the analysis of the near-side peak shapes study, see the corresponding analysis note [1].

The code of this analysis is found in AliRoot in PWGCF/Correlations/DPhi/AliAnalysisTaskPhiCorrelations.

## 1 Datasets

AliRoot version v5-04-01-AN has been used.

**p–Pb** Data: LHC12g\_pass2, runs 188359, 188362; ESDs.

MC: DPMJET LHC12g4b and HIJING LHC12g1

**pp 7 TeV** Data: LHC10d pass2, runs 125855, 125851, 125850, 125849, 125848, 125847, 125101, 125100, 125097, 125085, 125023, 126097, 126090, 126008, 126007, 126004, 125844, 125843, 125842, 125633, 125632, 125630, 125186, 125156, 125140, 125139, 125134, 125133, 122375, 126158, 126088, 126082, 126081, 126078, 126073, 125296, 122374; AODs AOD057

MC: LHC10f6a, AOD041

**pp 2.76 TeV** Data LHC11a pass 2 reconstruction with SDD, runs 146860, 146859, 146858, 146856, 146824, 146817, 146806, 146805, 146804, 146803, 146802, 146801, 146748, 146747, 146746; EDSs; only events with SDD used (i.e. fast cluster is rejected)

MC: Pythia LHC11b10a

## 2 Event Selection

Events have to pass the physics selection to select collision candidates (see below) and the reconstructed vertex has to be within  $\pm 10$  cm.

**p–Pb** The analysis requires the physics selection with the following p–Pb specific configuration:

```
gROOT->LoadMacro("$ALICE_ROOT/ANALYSIS/macros/PhysicsSelectionOADB_CINT5_pA.C");
AliOADBPhysicsSelection *oadb = OADBSelection_CINT5_VOAND();
<task>->GetPhysicsSelection()->SetCustomOADBObjects(oadb,0);
```

**pp** The kMB bit is used.

### 3 Track Selection

The main track selection are hybrid track cuts. For systematic comparisons, global tracks are used. The analysis uses tracks which are within  $|\eta| < 1.2$ .

**Hybrid Track Cuts** All tracks have to pass the following cuts:

```
fEsdTrackCuts = AliESDtrackCuts::GetStandardITSTPCTrackCuts2011(kFALSE);  
fEsdTrackCuts->SetName("Global Hybrid tracks, loose DCA");  
fEsdTrackCuts->SetMaxDCAToVertexXY(2.4);  
fEsdTrackCuts->SetMaxDCAToVertexZ(3.2);  
fEsdTrackCuts->SetDCAToVertex2D(kTRUE);  
fEsdTrackCuts->SetMaxChi2TPCCConstrainedGlobal(36);  
fEsdTrackCuts->SetClusterRequirementITS(AliESDtrackCuts::kSPD, AliESDtrackCuts::kOff);
```

Further, the track has to have a cluster in either of the SPD layer. If it does not have such a cluster, the primary vertex is used in the track fit by using the track parameters returned by:

```
esdTrack->GetConstrainedParam()
```

**Global Track Cuts** Standard global track cuts are used. To achieve a uniform  $\varphi$ -acceptance, alternatively to a cluster in the SPD, a hit in the first SDD layer is also accepted. This selection was already used in the analysis of the underlying event published in [2].

The track cuts are:

```
fEsdTrackCuts = AliESDtrackCuts::GetStandardITSTPCTrackCuts2011();  
fEsdTrackCuts->SetClusterRequirementITS(AliESDtrackCuts::kSPD, AliESDtrackCuts::kOff);  
  
fEsdTrackCutsExtra1 = new AliESDtrackCuts("SPD", "Require 1 cluster in SPD");  
fEsdTrackCutsExtra1->SetClusterRequirementITS(AliESDtrackCuts::kSPD, AliESDtrackCuts::kAny);  
  
fEsdTrackCutsExtra2 = new AliESDtrackCuts("SDD", "Require 1 cluster in first layer SDD");  
fEsdTrackCutsExtra2->SetClusterRequirementITS(AliESDtrackCuts::kSDD, AliESDtrackCuts::kFirst);
```

where a track has to pass `fEsdTrackCuts` and then either `fEsdTrackCutsExtra1` or `fEsdTrackCutsExtra2`.

### 4 Event Classes

In order to study the multiplicity dependence of the two-particle correlations the selected event sample is divided into four event classes. These classes are defined fractions of the analyzed event sample, based on cuts on the total charge deposited in the VZERO detector (V0M), and denoted “60–100%”, “40–60%”, “20–40%”, “0–20%” from the lowest to the highest multiplicity in the following. Table 1 shows the event-class definitions and the corresponding mean

charged-particle multiplicity densities ( $\langle dN_{\text{ch}}/d\eta \rangle$ ) within  $|\eta| < 0.5$ . These are obtained using the method presented in Ref. [3], and are corrected for acceptance and tracking efficiency as well as contamination by secondary particles. These numbers have been provided by Ruben Shahoyan.

We also calculate the mean numbers of primary charged particles with  $p_{\text{T}} > 0.5 \text{ GeV}/c$  within the pseudorapidity range  $|\eta| < 1.2$ . These are corrected for the detector acceptance, track-reconstruction efficiency and contamination (see Section 7).

Event class	V0M range (a.u.)	$\langle dN_{\text{ch}}/d\eta \rangle  _{ \eta  < 0.5}$ $p_{\text{T}} > 0 \text{ GeV}/c$	$\langle N_{\text{trk}} \rangle  _{ \eta  < 1.2}$ $p_{\text{T}} > 0.5 \text{ GeV}/c$
60–100%	< 138	$6.6 \pm 0.2$	$6.4 \pm 0.2$
40–60%	138–216	$16.2 \pm 0.4$	$16.9 \pm 0.6$
20–40%	216–318	$23.7 \pm 0.5$	$26.1 \pm 0.9$
0–20%	> 318	$34.9 \pm 0.5$	$42.5 \pm 1.5$

Table 1: Definition of the event classes as fractions of the analyzed event sample and their corresponding  $\langle dN_{\text{ch}}/d\eta \rangle$  within  $|\eta| < 0.5$  and the mean numbers of charged particles within  $|\eta| < 1.2$  and  $p_{\text{T}} > 0.5 \text{ GeV}/c$ . The given uncertainties are systematic as the statistical uncertainties are negligible. These are estimated as described in Ref. [3].

Further, we use the ZNA and the SPD to split the data into event classes. For both, VZERO and SPD, the centrality framework is used. For the ZNA the following limits, provided by Chiara Oppedisano, were used:

Event class	ZNA range (a.u.)
60–100%	< 413
40–60%	413–563
20–40%	563–681
0–20%	> 681

## 5 Correlation Function

For a given event class, the two-particle correlation between pairs of trigger and associated charged particles is measured as a function of the azimuthal difference  $\Delta\varphi$  (defined within  $-\pi/2$  and  $3\pi/2$ ) and pseudorapidity difference  $\Delta\eta$ . The correlation is expressed in terms of the associated yield per trigger particle for different intervals of trigger and associated transverse momentum,  $p_{\text{T},\text{trig}}$  and  $p_{\text{T},\text{assoc}}$ , respectively, and  $p_{\text{T},\text{assoc}} < p_{\text{T},\text{trig}}$ . The associated yield per

trigger particle is defined as

$$\frac{1}{N_{\text{trig}}} \frac{d^2 N_{\text{assoc}}}{d\Delta\eta d\Delta\varphi} = \frac{S(\Delta\eta, \Delta\varphi)}{B(\Delta\eta, \Delta\varphi)} \quad (1)$$

where  $N_{\text{trig}}$  is the total number of trigger particles in the event class and  $p_{T,\text{trig}}$  interval. The signal distribution  $S(\Delta\eta, \Delta\varphi) = 1/N_{\text{trig}} d^2 N_{\text{same}}/d\Delta\eta d\Delta\varphi$  is the associated yield per trigger particle for particle pairs from the same event. In a given event class and  $p_T$  interval, the sum over the events is performed separately for  $N_{\text{trig}}$  and  $d^2 N_{\text{same}}/d\Delta\eta d\Delta\varphi$  before their ratio is computed.

Note, that this definition is different from the one used by CMS in Ref. [4], where  $S(\Delta\eta, \Delta\varphi)$  is calculated per event and then averaged. The method used in our analysis does not induce an inherent multiplicity dependence (see Section 6) in the pair yields, which is important for the subtraction method discussed in Section 8.

The background distribution  $B(\Delta\eta, \Delta\varphi) = \alpha d^2 N_{\text{mixed}}/d\Delta\eta d\Delta\varphi$  corrects for pair acceptance and pair efficiency. It is constructed by correlating the trigger particles in one event with the associated particles from other events in the same event class and within the same 2 cm wide  $z_{\text{vtx}}$  interval (each event is mixed with 5–20 events).

The factor  $\alpha$  is chosen to normalize the background distribution such that it is unity for pairs where both particles go into approximately the same direction (i.e.  $\Delta\varphi \approx 0, \Delta\eta \approx 0$ ). In fact due to the cut on pairs which are spatially close (see next paragraph)  $S$  and  $B$  have a dip around  $\Delta\varphi \approx 0, \Delta\eta \approx 0$ . Therefore,  $\alpha$  is estimated from the plateau along  $\Delta\varphi \approx 0$  but excluding  $\Delta\eta \approx 0$ . This is feasible because there is a rather flat acceptance as function of  $\Delta\varphi$ . Finally, a small correction needs to be applied to  $\alpha$  due to the finite binning: the bin(s) at  $\Delta\eta \approx 0$  are of finite size and therefore are an integral over some range of the triangle instead of just being the tip of it. This correction can be corrected analytically  $(-0.5/\max(\eta) \cdot \text{binWidthEta} + 1)$  where  $\max(\eta)$  is the single-particle  $\eta$  cut, and  $\text{binWidthEta}$  is the widths of the bins in  $\eta$ .

To account for different pair acceptance and pair efficiency as a function of  $z_{\text{vtx}}$ , the yield defined by Eq. 1 is constructed for each  $z_{\text{vtx}}$  interval. The final per-trigger yield is obtained by calculating the weighted average of the  $z_{\text{vtx}}$  intervals.

When constructing the signal and background distributions, the trigger and associated particles are required to be separated by  $|\Delta\varphi_{\text{min}}^*| > 0.02$  and  $|\Delta\eta| > 0.02$ , where  $\Delta\varphi_{\text{min}}^*$  is the minimal azimuthal distance at the same radius between the two tracks within the active detector volume after accounting for the bending due to the magnetic field [5]. This procedure is applied to avoid a bias due to the reduced efficiency for pairs with small opening angles and leads to an increase in the associated near-side peak yield of 0.4–0.8% depending on  $p_T$ .

Furthermore, particle pairs are removed which are likely to stem from a  $\gamma$ -conversion, or a  $K_s^0$  or  $\Lambda$  decay, by a cut on the invariant mass of the pair (the electron, pion, or pion/proton mass is assumed, respectively). The applied cuts are  $m_{\text{inv}} < 0.04 \text{ GeV}/c$  ( $\gamma$ -conversion) and

$\pm 0.02 \text{ GeV}/c$  around the mass of the  $K_s^0$  or  $\Lambda$ . The effect on the near-side peak yields is less than 2%.

## 6 Comparison with Alternative Averaging Procedures

As mentioned in the previous section, the ratio between the average number of pairs and the average number of trigger particles does not induce an inherent multiplicity dependence, whereas, in the case of symmetric  $p_T$ -bins, the average of event-by-event ratios of the two quantities has a trivial multiplicity dependence. The easiest way to discuss the dependence is to consider correlations in event  $i$  induced by  $N^i$  sources of particle emission each emitting particles with a number distribution  $P(n)$ .

**Ratio of Averages** Ration of averages can be written as:

$$\begin{aligned} \frac{\langle N_{pair} \rangle}{\langle N_{trig} \rangle} &= \frac{\sum_{i=1}^{N_{evt}} \sum_{j=1}^{N_{source}^i} \frac{1}{2} n_{ij} (n_{ij} - 1)}{\sum_{i=1}^{N_{evt}} \sum_{j=1}^{N_{source}^i} n_{ij}} \\ &= \frac{N_{evt} \langle N_{source} \rangle \frac{1}{2} \langle n(n-1) \rangle}{N_{evt} \langle N_{source} \rangle \langle n \rangle} \\ &= \frac{1}{2} \frac{\langle n(n-1) \rangle}{\langle n \rangle} \end{aligned} \quad (2)$$

The results does not depend on the distribution of  $N_{source}^i$ .

**Average of Ratios**

$$\left\langle \frac{N_{pair}}{N_{trig}} \right\rangle = \frac{1}{N_{evt}} \sum_i \frac{\sum_{j=1}^{N_{source}^i} \frac{1}{2} n_{ij} (n_{ij} - 1)}{\sum_{j=1}^{N_{source}^i} n_{i,j}} \quad (3)$$

It is impossible to simplify this expression for the general case. The result depends on the distribution of number of sources. This can be seen by considering two limiting cases.

(1)  $N_{source} = 1$

$$\left\langle \frac{N_{pair}}{N_{trig}} \right\rangle = \frac{1}{2} \langle n-1 \rangle |_{n>0} = \frac{1}{2} \frac{\langle n \rangle}{1 - p_0} - 1 \quad (4)$$

The average of ratios measures half of the number of additional particles under the condition to have at least one trigger particle.

(2)  $N_{source} \gg 1$  In this case the source average and the event average are equal and the average of ratios is equal to the ratio of averages.

$$\begin{aligned} \frac{N_{pair}}{N_{trig}} &= \frac{1}{N_{evt}} \sum_i \frac{\sum_{j=1}^{N_{source}^i} \frac{1}{2} n_{i,j} (n_{i,j} - 1)}{\sum_{j=1}^{N_{source}^i} n_{i,j}} \\ &= \frac{1}{2} \frac{\langle n(n-1) \rangle}{\langle n \rangle} \end{aligned} \quad (5)$$

The limit of the expression for small  $\langle n \rangle$  is

$$\frac{\langle n \rangle}{1 - p_0} - 1$$

twice the value obtained in case (1).

## 7 Corrections

A combined single-particle efficiency and contamination correction is computed as a function of  $\eta$ ,  $p_T$  and  $z_{\text{vtx}}$ . We found no significant multiplicity dependence of this correction. Fig. 1 shows tracking efficiency and contamination correction as projections to different axes for hybrid track cuts. Fig. 2 shows the same for global track cuts.

The corrections are applied as weights for each particle, i.e. each associated particle and each trigger particle is weighted. Therefore, each pair is weighted with the combined correction factor. The weighting of trigger particles drops out in a given bin, but is needed because the correction changes by up to 3% within the wide bins used in the final results (see Fig. 1).

### 7.1 MC Closure Test

The corrections procedure is exercised on MC events. Fig. 3 and 4 shows the ratio of per-trigger yield for MC truth and corrected reconstructed MC. The differences are used in the systematic uncertainties (non closure).

We also apply HLJING corrections to DPMJET with similar results.

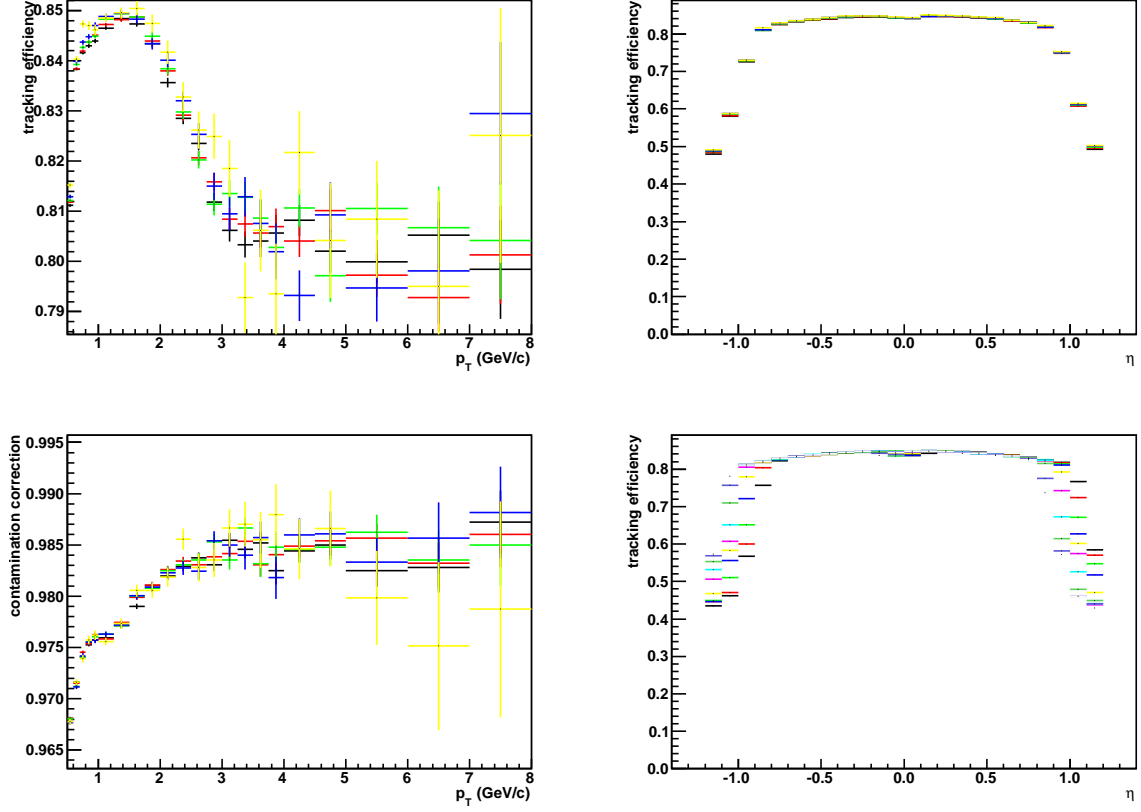


Figure 1: Tracking efficiency projected to  $p_T$  (top left) within  $|\eta| < 0.9$  and projected to  $\eta$  within  $0.5 < p_T < 8$  GeV/c (top right). Contamination correction projected to  $p_T$  (bottom left) within  $|\eta| < 0.9$ . In these three panels the different colors show different multiplicity ranges: black (0–20%), red (20–40%), green (40–60%), blue (60–80%), yellow (80–100%). Bottom right panel: tracking efficiency projected to  $\eta$  within  $0.5 < p_T < 8$  GeV/c for different 2 cm wide  $z_{\text{vtx}}$ -ranges starting from  $-10 < z_{\text{vtx}} < -8$  represented by the colors: black, red, green, blue, yellow, pink, light blue, dark green, violet, greenblue. Extracted from DPMJET.



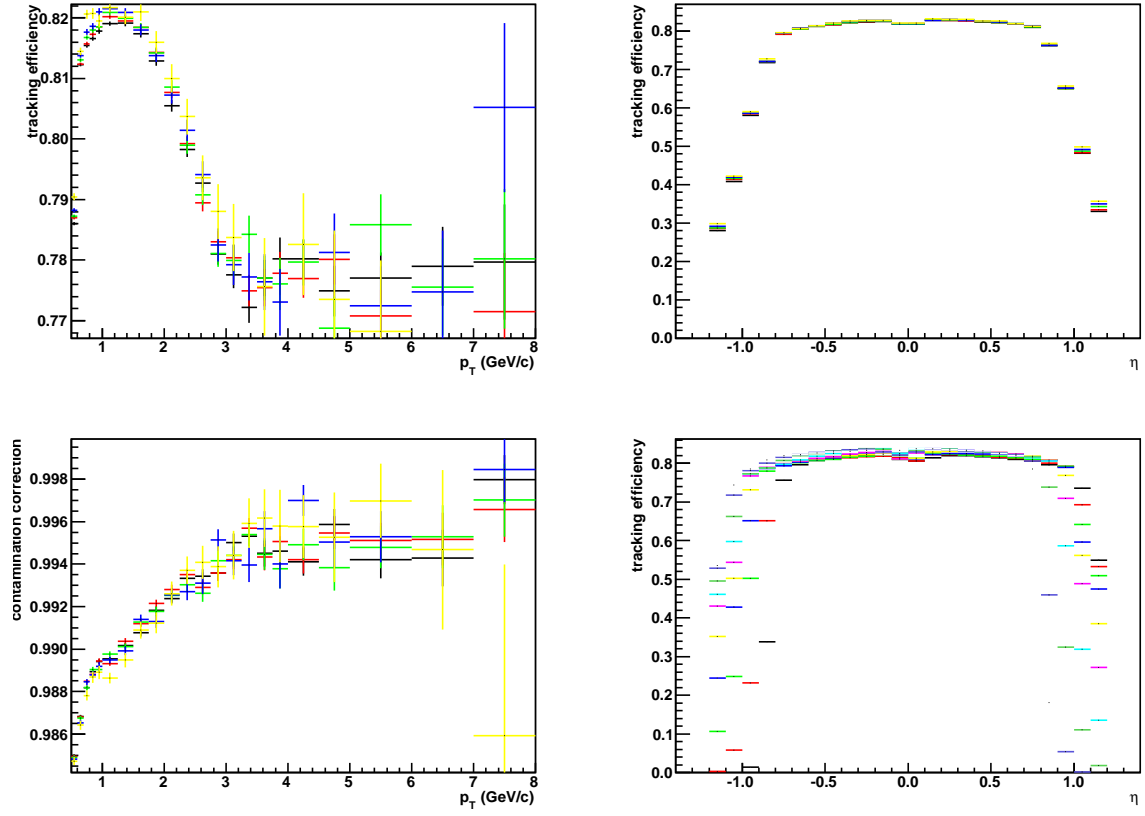


Figure 2: Same as Fig. 1 but for global track cuts.

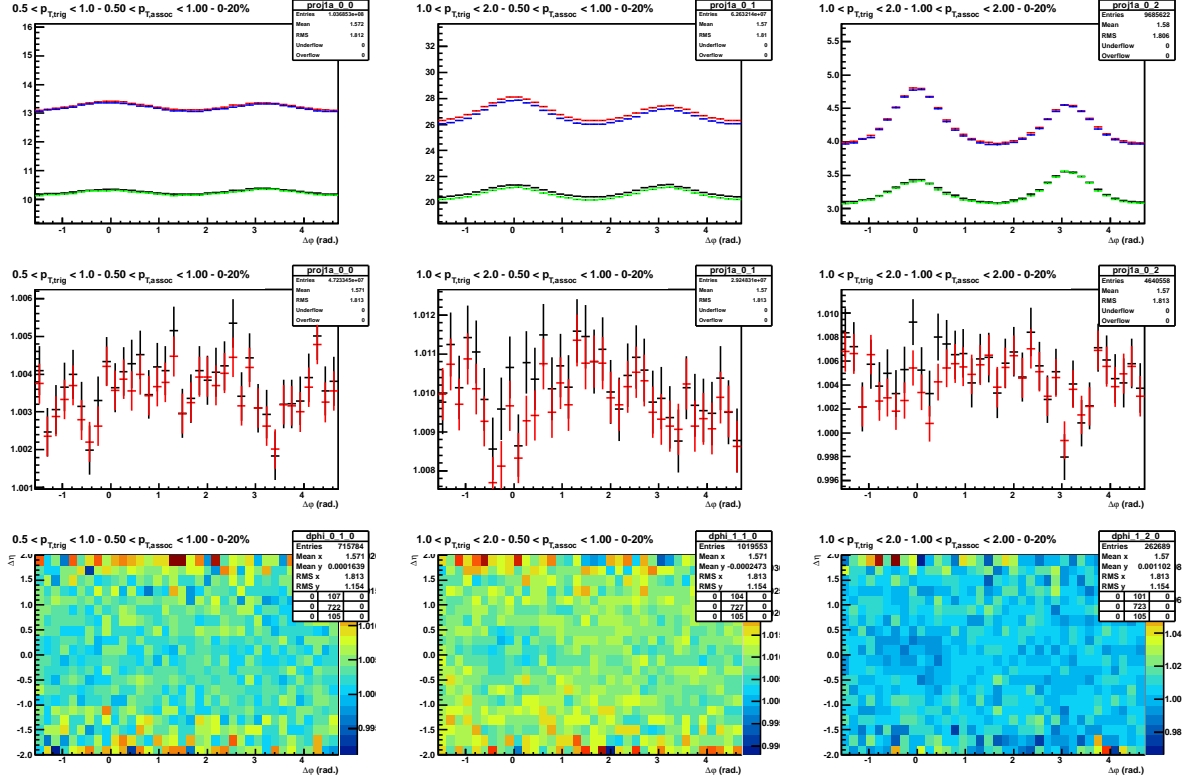


Figure 3: MC closure test with DPMJET. The first row shows the projection to  $\Delta\varphi$  for all  $\Delta\eta$  on MC truth (red) and corrected (blue) as well as for  $0.5 < |\Delta\eta| < 1.8$  on MC truth (black) and corrected (green). The second row shows the ratio of MC level and corrected for the full  $\Delta\eta$  (black) and the restricted one (red). The third row shows the ratio of MC truth and corrected in two dimensions.

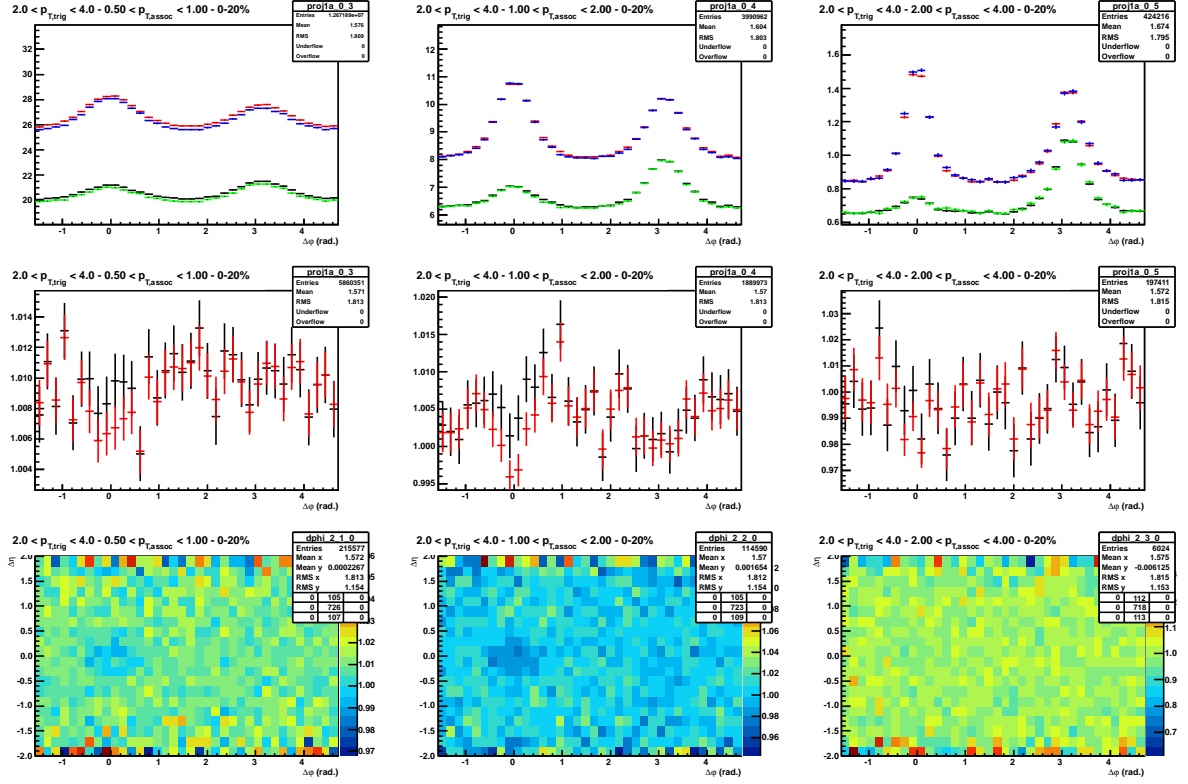


Figure 4: Same as Fig. 3 for further  $p_T$  bins.

## 8 Subtraction Procedure

The corrected per-trigger yield is presented for different  $p_T$  bins and multiplicity classes in Figures 5–8.

To quantify the change from low to high multiplicity event classes, we subtract the per-trigger yield of the lowest (60–100%) from that of the higher multiplicity classes. The resulting distribution in  $\Delta\varphi$  and  $\Delta\eta$  for the 0–20% event classes are shown in Fig. 9. Note that the baseline of those plots is somewhat arbitrary, i.e. it is the difference in baseline of the high and the low multiplicity class.

Fig. 10 shows the projection of the 2d distributions to  $\Delta\eta$  in different ranges of  $\Delta\varphi$ .

Fig. 11 shows the projection to  $\Delta\varphi$  averaged over  $0.8 < |\Delta\eta| < 1.8$  on the near side and  $|\Delta\eta| < 1.8$  on the away side. The figure also shows fits with

$$1/N_{\text{trig}} dN_{\text{assoc}}/d\Delta\varphi = a_0 + 2a_2 \cos(2\Delta\varphi) + 2a_3 \cos(3\Delta\varphi) \quad (6)$$

with and without the  $2a_3 \cos(3\Delta\varphi)$  term. The shown baseline is taken from the minimum of the fit including the  $a_3$  term.

### 8.1 Subtraction Procedure with pp Collisions

Despite the difference in center-of-mass energy, we subtract the correlation in pp events at 7 TeV from the correlation in events with low multiplicity (60–100%). The projections onto  $\Delta\varphi$  are shown in Fig. 12. No significant structures remain and we conclude that the double-ridge structure is not present in the low-multiplicity event class.

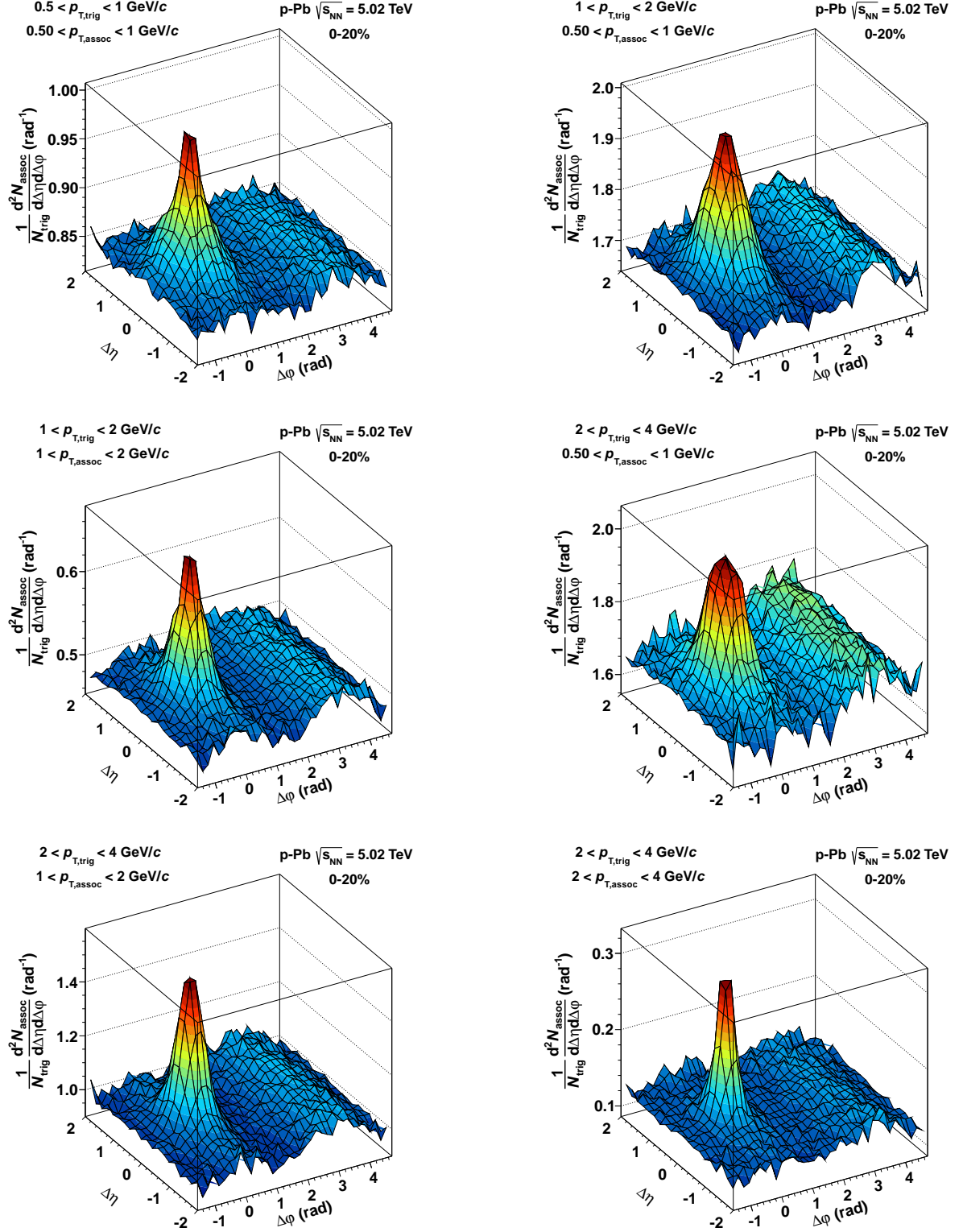


Figure 5: Associated yield per trigger particle in  $\Delta\phi$  and  $\Delta\eta$  for different  $p_{\text{T}}$  bins (see labels) for the 0–20% multiplicity class.

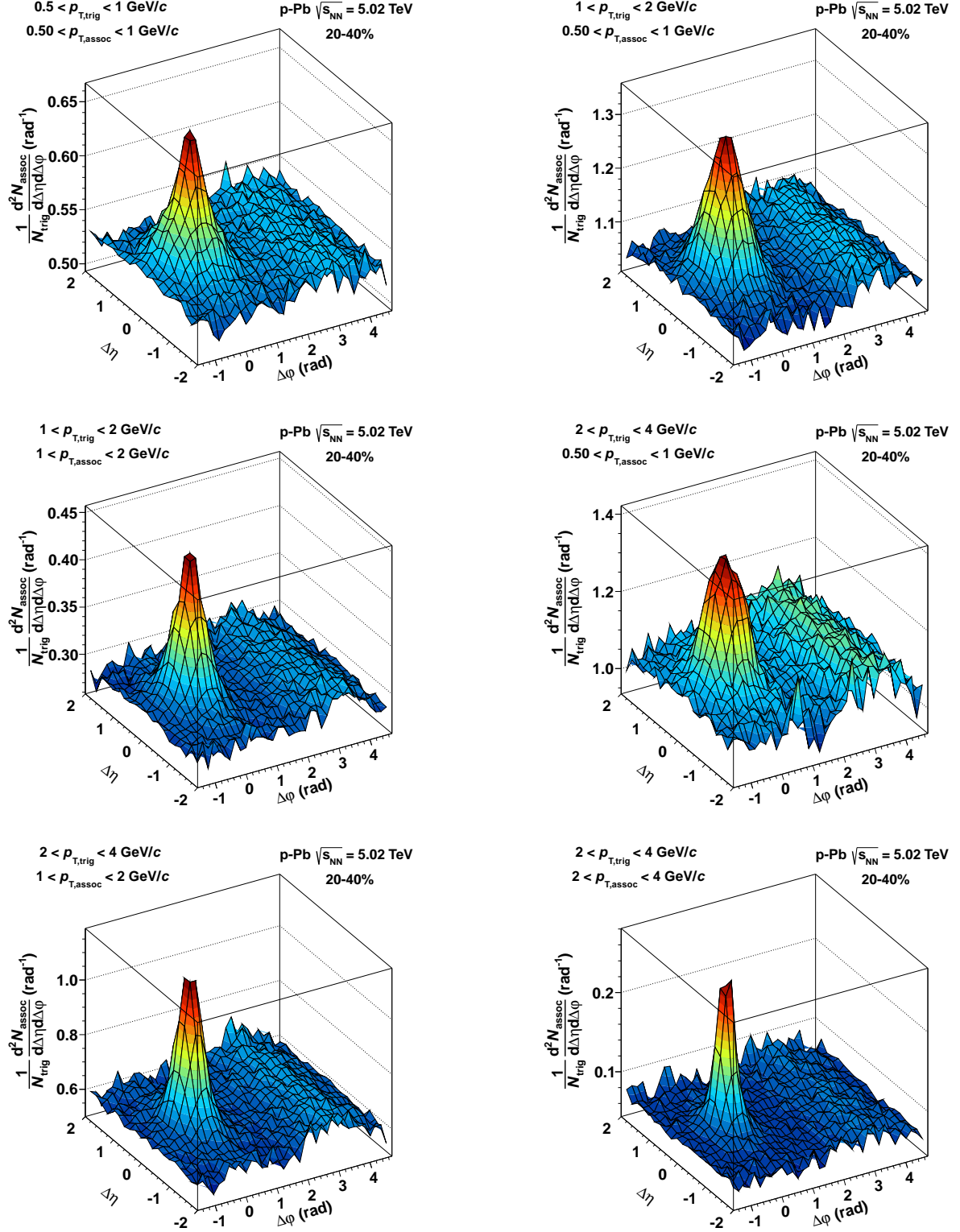


Figure 6: Associated yield per trigger particle in  $\Delta\phi$  and  $\Delta\eta$  for different  $p_{\text{T}}$  bins (see labels) for the 20–40% multiplicity class.

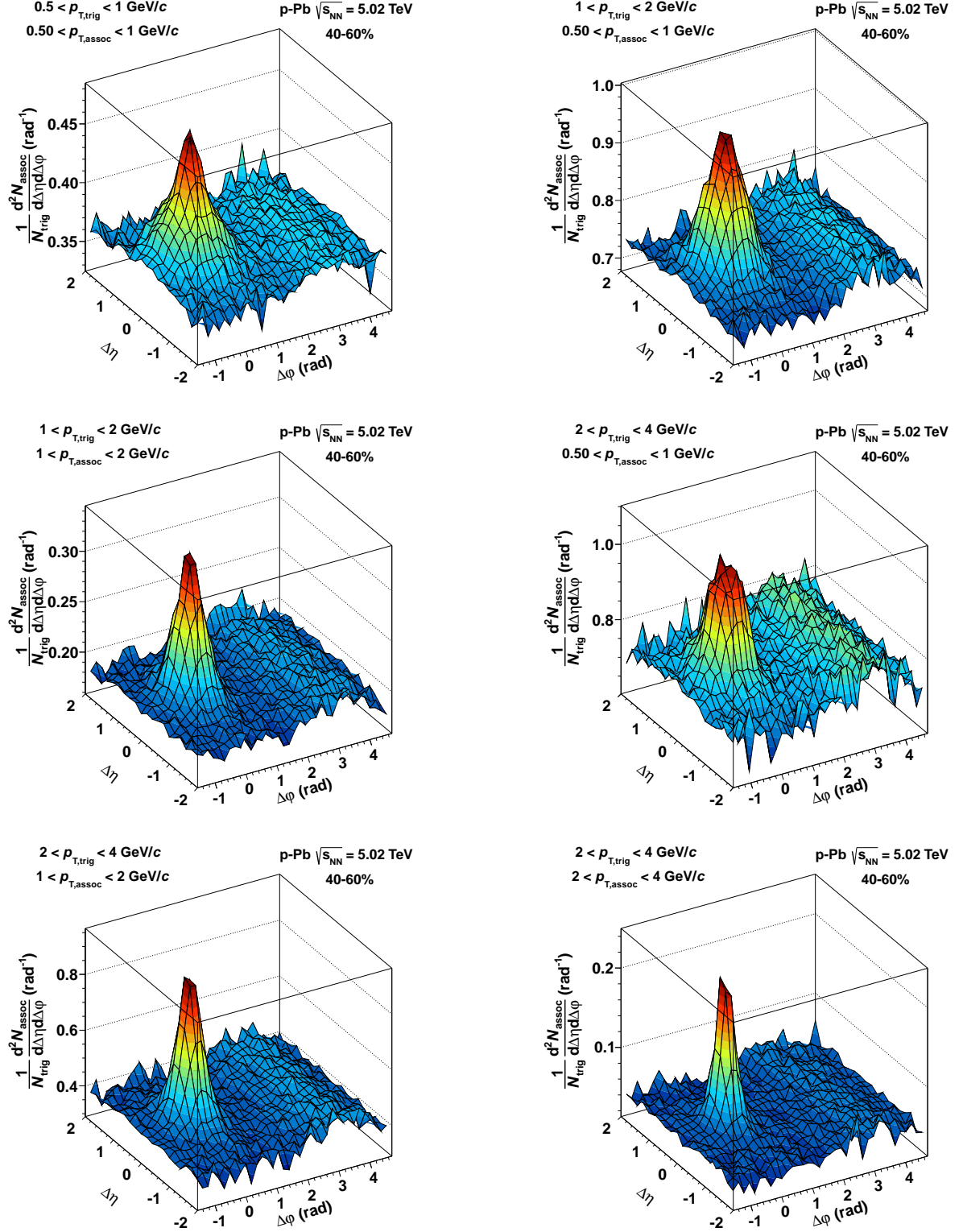


Figure 7: Associated yield per trigger particle in  $\Delta\varphi$  and  $\Delta\eta$  for different  $p_T$  bins (see labels) for the 40–60% multiplicity class.



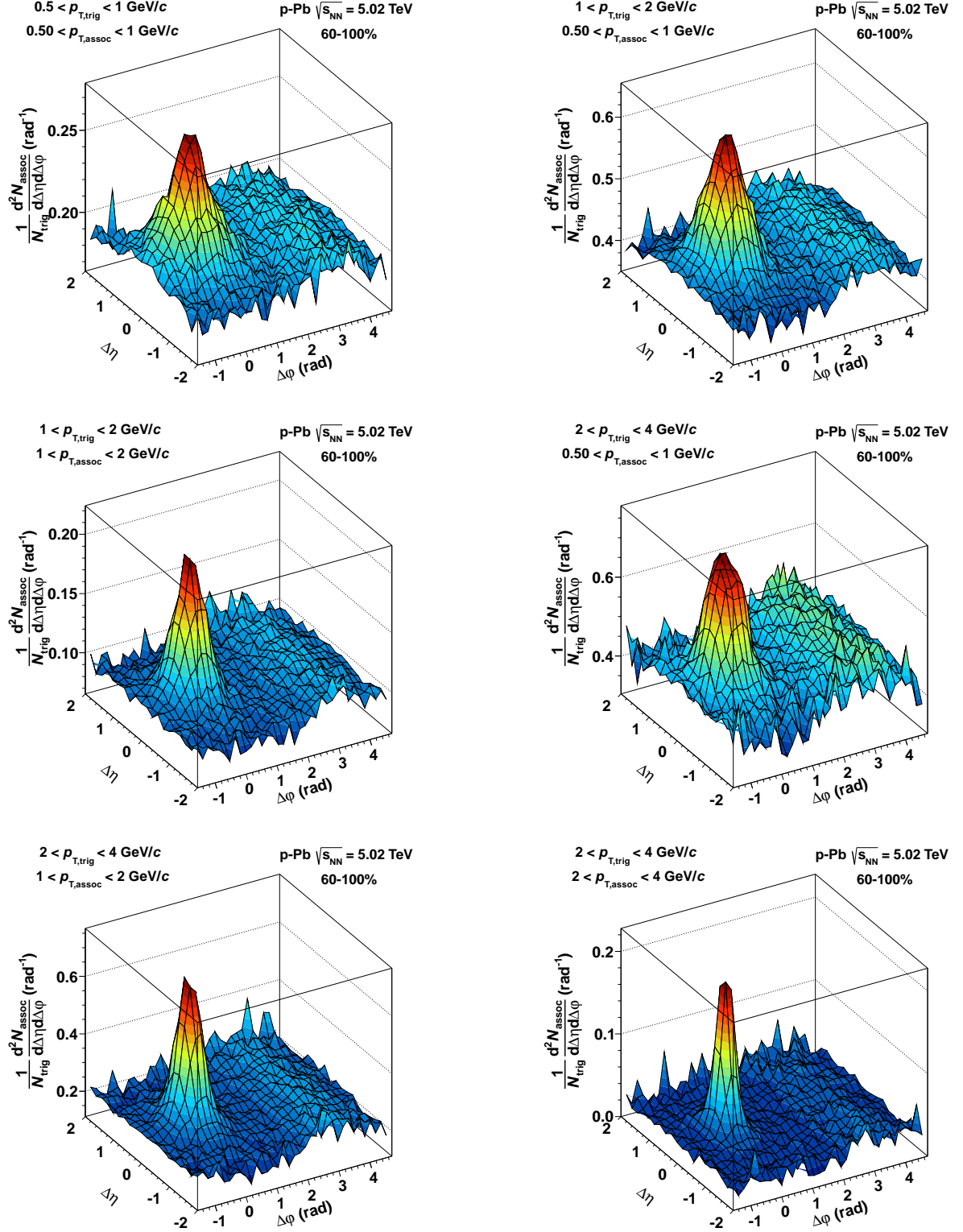


Figure 8: Associated yield per trigger particle in  $\Delta\phi$  and  $\Delta\eta$  for different  $p_T$  bins (see labels) for the 60–100% multiplicity class.



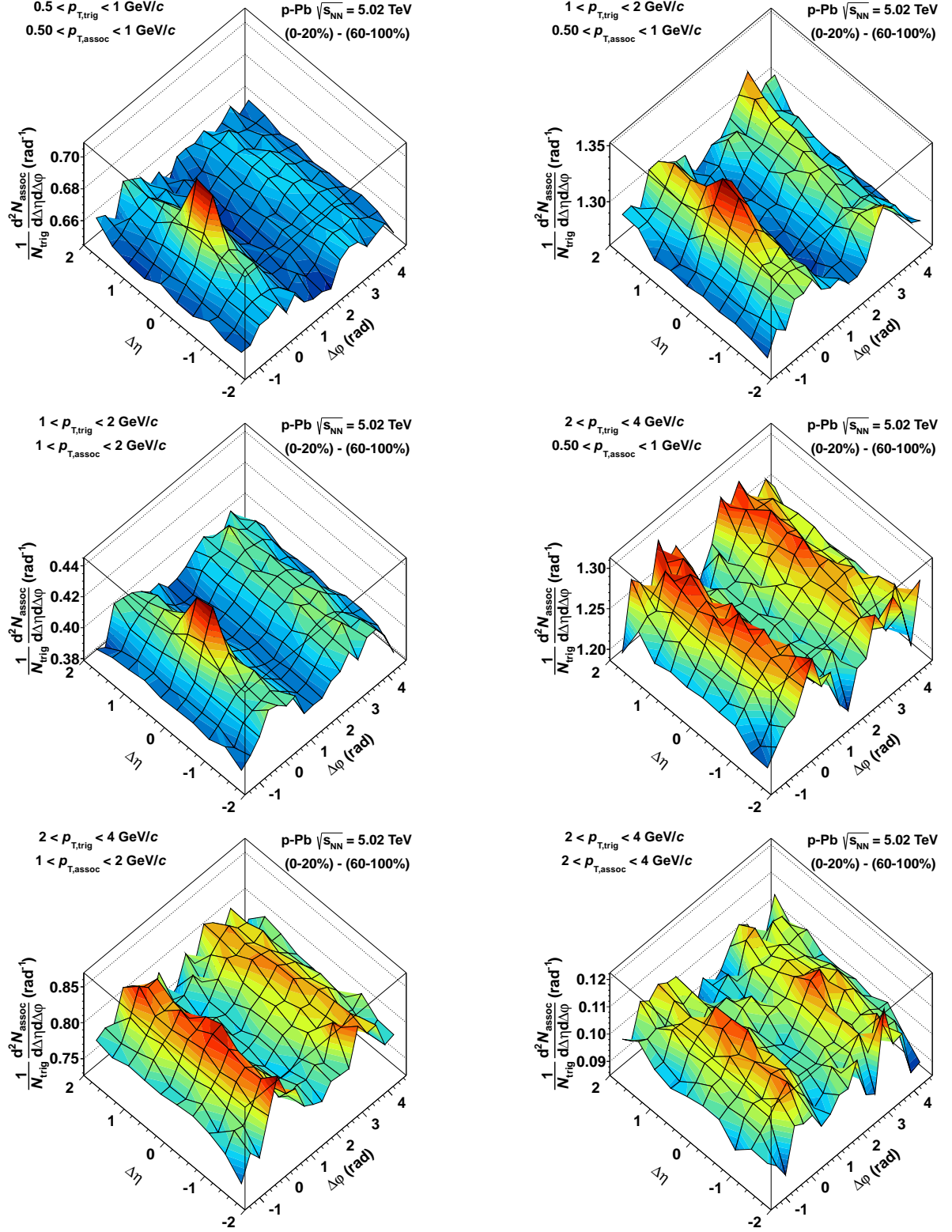


Figure 9: Associated yield per trigger particle in  $\Delta\phi$  and  $\Delta\eta$  for different  $p_T$  bins (see labels) for the 0–20% multiplicity class, after subtraction of the associated yield obtained in the 60–100% event class.

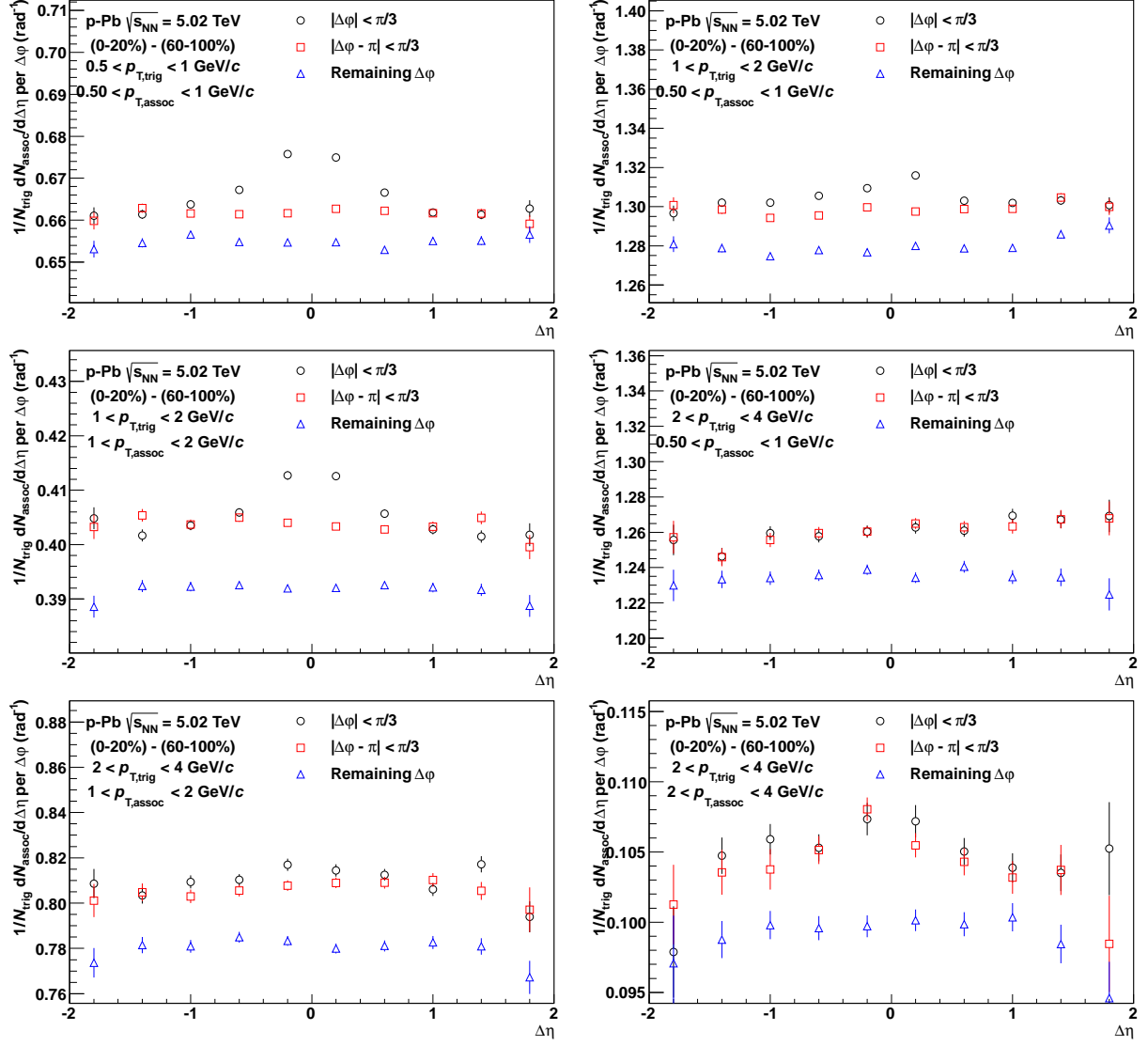


Figure 10: Projections of Fig. 9 onto  $\Delta\eta$  averaged over  $|\Delta\varphi| < \pi/3$  (black circles),  $|\Delta\varphi - \pi| < \pi/3$  (red squares), and the remaining area (blue triangles,  $\Delta\varphi < -\pi/3$ ,  $\pi/3 < \Delta\varphi < 2\pi/3$  and  $\Delta\varphi > 4\pi/3$ ).

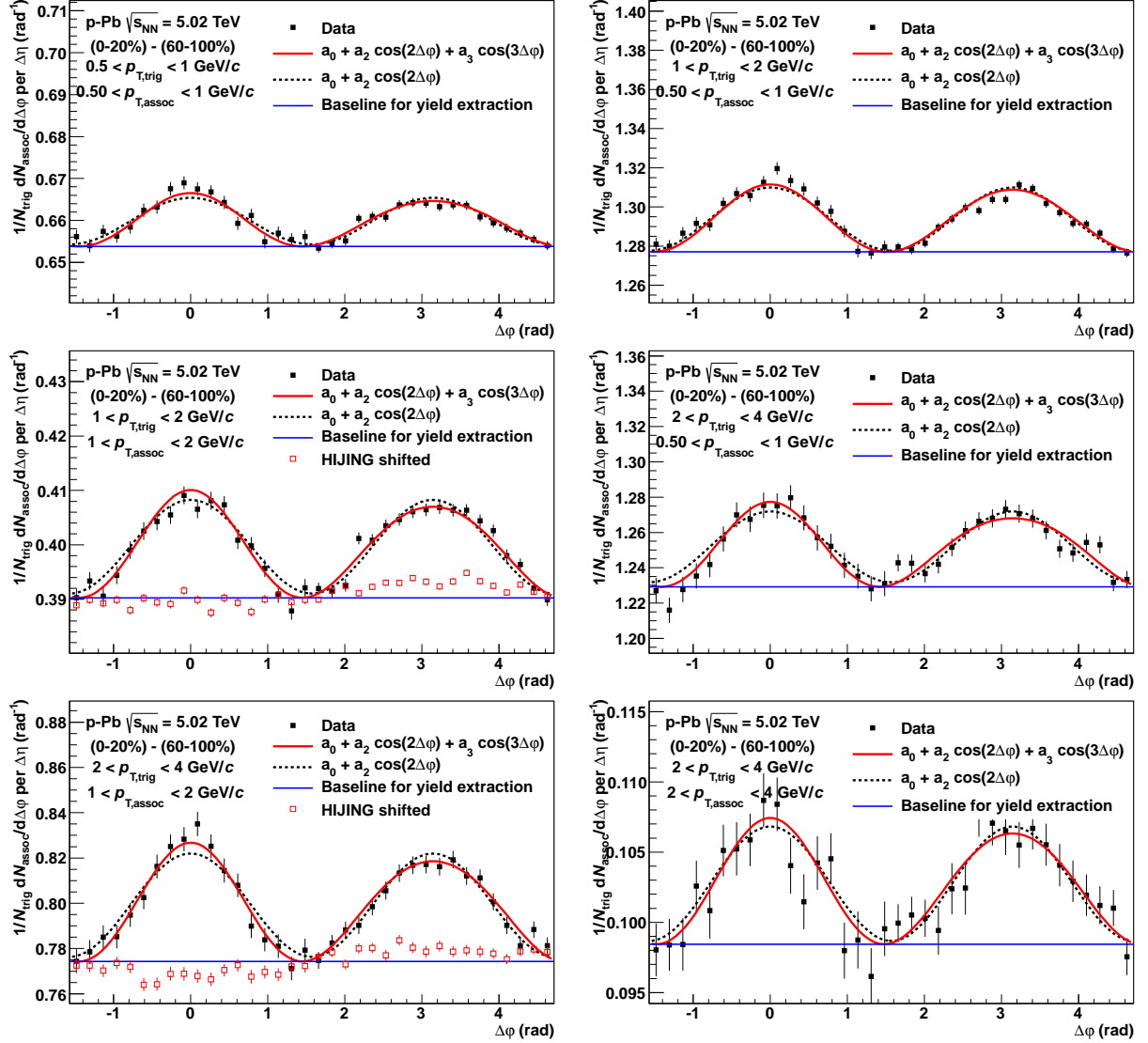


Figure 11: Projections of Fig. 9 onto  $\Delta\varphi$  averaged over  $0.8 < |\Delta\eta| < 1.8$  on the near side and  $|\Delta\eta| < 1.8$  on the away side. Superimposed are fits containing a  $\cos(2\Delta\varphi)$  shape alone (black dashed line) and a combination of  $\cos(2\Delta\varphi)$  and  $\cos(3\Delta\varphi)$  shapes (red solid line). The blue horizontal line shows the baseline obtained from the latter fit which is used for the yield calculation. In some bins also shown for comparison is the subtracted associated yield when the same procedure is applied on HIJING shifted to the same baseline.

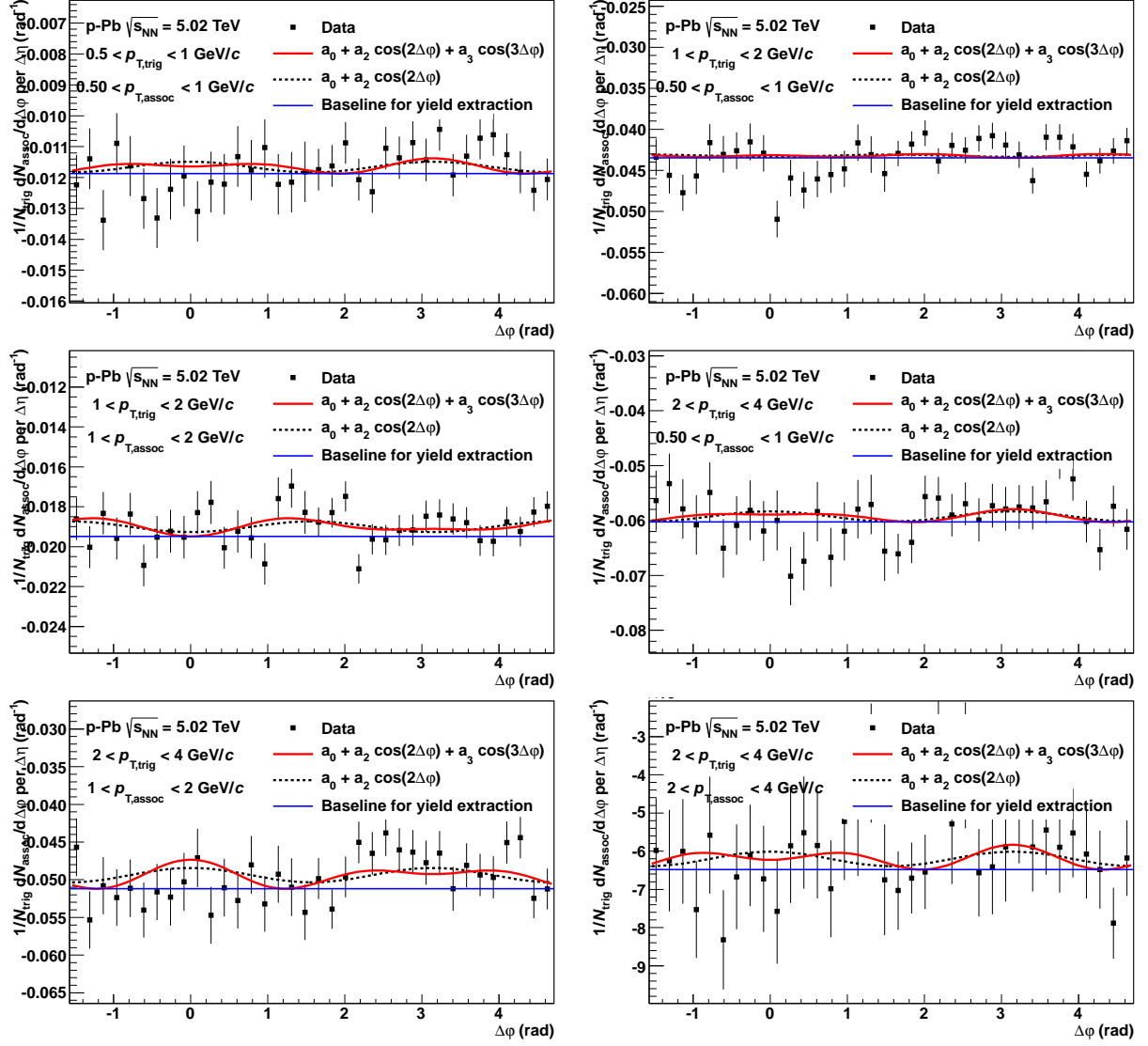


Figure 12: Same as Fig. 11 but for the event class 60–100% from which the correlation in pp events at 7 TeV has been subtracted.

## 9 $v_n$ Extraction

The fit parameters  $a_2$  and  $a_3$  of the fit shown in Fig. 11 are a measure of the absolute modulation in the subtracted per-trigger yield and characterize a modulation relative to the baseline  $b$  in the higher multiplicity class assuming that such a modulation is not present in the 60–100% event class. Therefore, the Fourier coefficients  $v_n$  of the corresponding single-particle distribution, commonly used in the analysis of particle correlations in nucleus–nucleus collisions, can be obtained in bins where the  $p_{T,\text{trig}}$  and  $p_{T,\text{assoc}}$  intervals are identical using

$$v_n = \sqrt{a_n/b}. \quad (7)$$

The baseline  $b$  is evaluated in the higher-multiplicity class in the region  $|\Delta\varphi - \pi/2| < 0.2$ , corrected for the fact that it is obtained in the minimum of the fit function.

The coefficients are presented in Fig. 13.

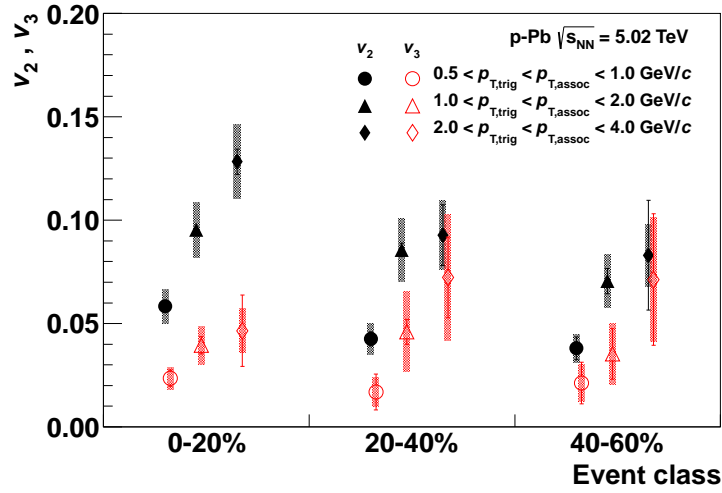


Figure 13:  $v_n$  coefficients. Systematic uncertainties are discussed further below.

## 10 Yield Extraction

From Fig. 11, ridge yields are extracted. This is done by integrating the data points above the baseline from  $-\pi/2$  to  $\pi/2$  for the near side and from  $\pi/2$  to  $3\pi/2$  for the away side. These are presented in Fig. 14.

## 11 Width

From the baseline-subtracted per-trigger yields the square root of the variance,  $\sigma$ , within  $|\Delta\varphi| < \pi/2$  and  $\pi/2 < \Delta\varphi < 3\pi/2$  for the near-side and away-side region, respectively, is calculated. These are presented in Fig. 15.

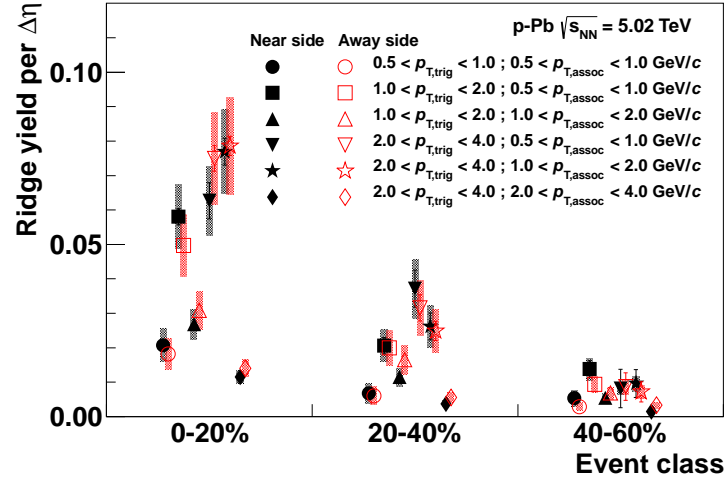


Figure 14: Ridge yields. Systematic uncertainties are discussed further below.

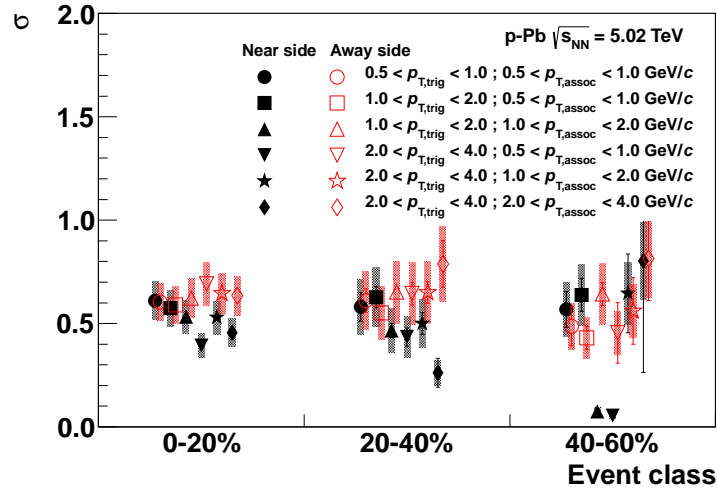


Figure 15: Width. Systematic uncertainties are discussed further below.

## 12 Systematic Uncertainties

This section discusses first how the uncertainties are evaluated; then the plots which show the different effect are shown followed by a table summarizing the uncertainties. Single uncertainties are extracted as maximum deviations from the “default” case avoiding effects of statistical fluctuations where required. The single uncertainties are then used symmetrically and added in quadrature for the final systematic uncertainties.

### 12.1 Track Cuts

The analysis is done with two different sets of cuts (see above): hybrid track cuts and global track cuts.

### 12.2 MC Generator and Corrections

Correction factors extracted from DPMJET simulations are used to correct events simulated with HIJING. The corrected per-trigger yields are compared to the input MC per-trigger yield. The two-dimensional ratio (as function of  $\Delta\eta$  and  $\Delta\varphi$ , per  $p_T$  bin; no multiplicity dependence is observed) is applied to the corrected per-trigger yields from data. All quantities are extracted with and without this MC non closure effect applied and the difference is taken into account for the systematic uncertainties.

### 12.3 Baseline Evaluation

The baseline (blue line in e.g. Fig. 11) is extracted either from the fit function (Eq. (6)) or taken as the minimum of a parabolic function fitted within  $|\Delta\varphi - \pi/2| < 1$ .

### 12.4 Residual Near-Side Peak

A potential bias due to the above-mentioned incomplete near-side peak subtraction is evaluated in the following way:

- the size of the near-side exclusion region is changed from  $|\Delta\eta| < 0.8$  to  $|\Delta\eta| < 1.2$ ;
- the residual near-side peak above the ridge is also subtracted from the away side by mirroring it at  $\Delta\varphi = \pi/2$  accounting for the general  $p_T$ -dependent difference of near-side and away-side jet yields due to the kinematic constraints and the detector acceptance, which is evaluated using the lowest multiplicity class (see Fig. 16);
- the lower multiplicity class is scaled before the subtraction such that no residual near-side peak above the ridge remains. The scaling factors are 1–26% depending on the bin.

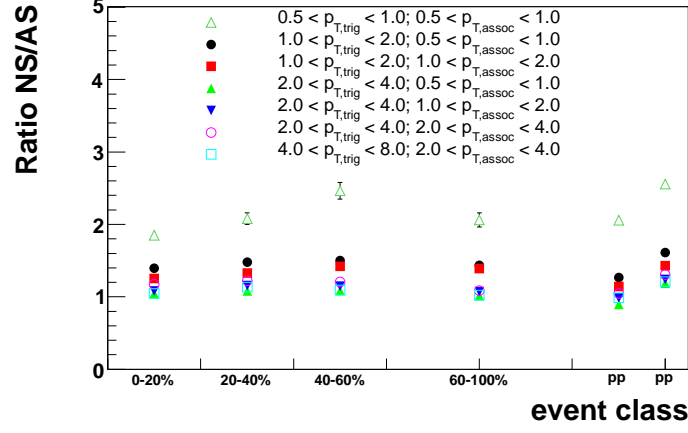


Figure 16: Ratio of NS and AS yield for different  $p_T$  bins and multiplicity classes. NS and AS yields are extracted from the 2D correlation function in the range  $|\Delta\eta| < 1.8$ ,  $|\Delta\varphi| < 1.0$  (NS) and  $|\pi - \Delta\varphi| < 1.0$  (AS), respectively. The yields are integrated after subtraction of the uncorrelated background that is evaluated at sufficient separation from the NS jet peak and the NS and AS ridges (i.e. in the region where  $\sqrt{\Delta\varphi^2 + \Delta\eta^2} > 1.6$ ,  $|\Delta\varphi| > 1.35$  and  $|\pi - \Delta\varphi| > 1.35$ ).

## 12.5 Effect of Systematic Uncertainties

Figures 17–20 show the effect of the different uncertainties on the observables.



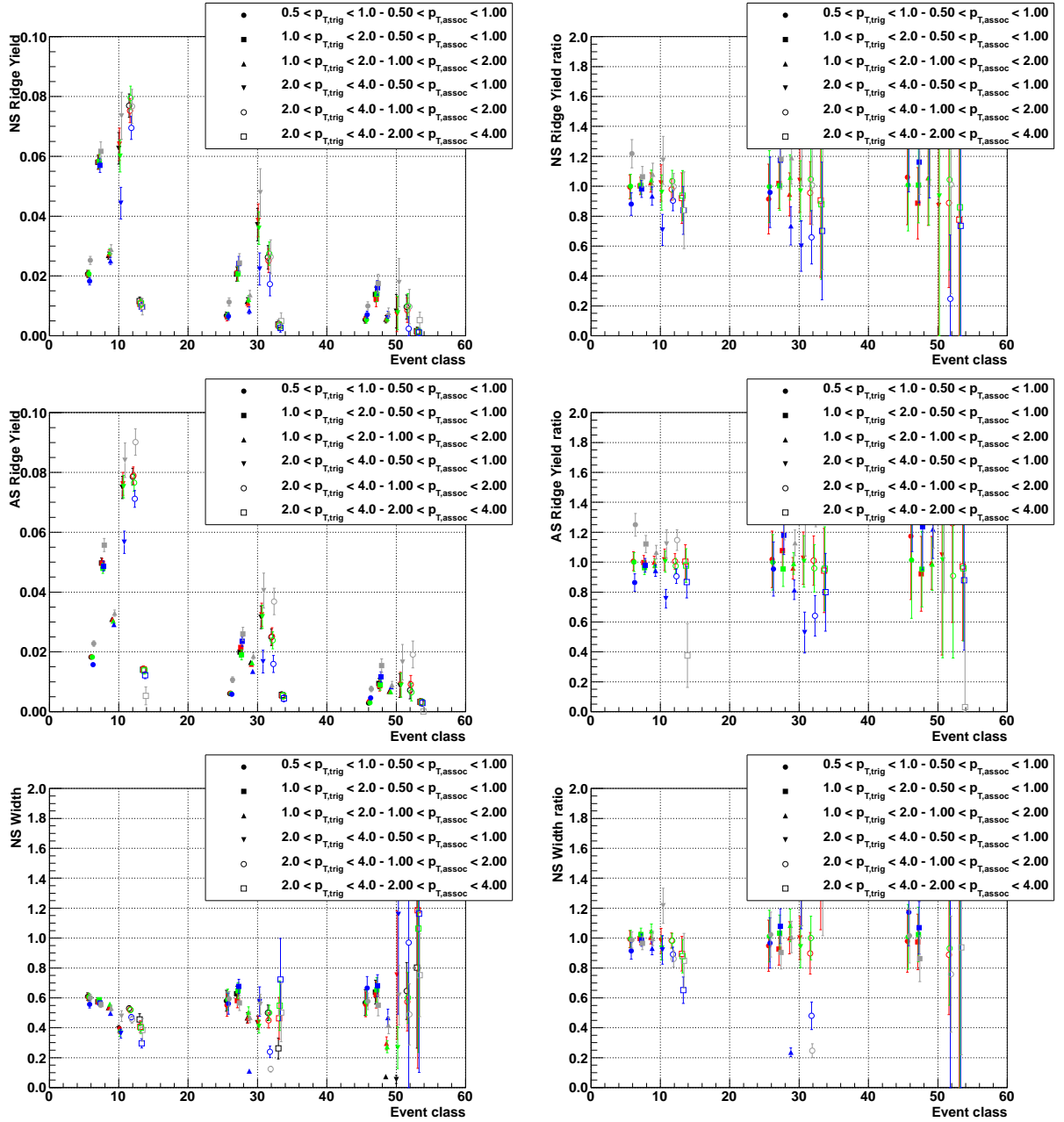


Figure 17: Systematic uncertainties evaluation. Shown are: default (black), change in track cuts (red), MC generator and non closure (green) and baseline (blue). Further in grey (not used for the final uncertainties) is the result when using 80–100% as peripheral class instead of 60–100%. Left panels show the effect on an observable; the right panels show the ratio to the default.

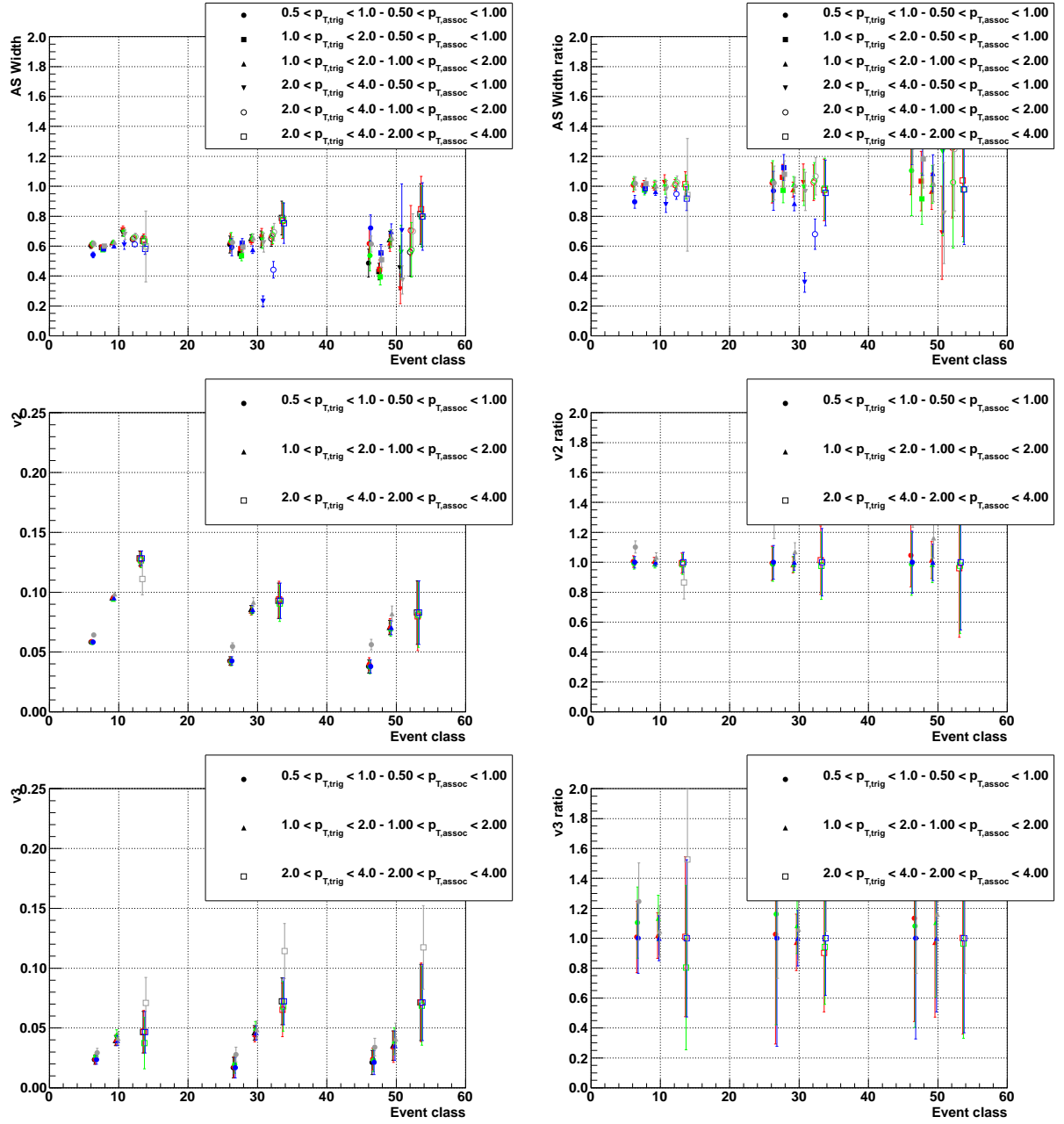


Figure 18: Systematic uncertainties evaluation. Shown are: default (black), change in track cuts (red), MC generator and non closure (green) and baseline (blue). Further in grey (not used for the final uncertainties) is the result when using 80–100% as peripheral class instead of 60–100%. Left panels show the effect on an observable; the right panels show the ratio to the default.

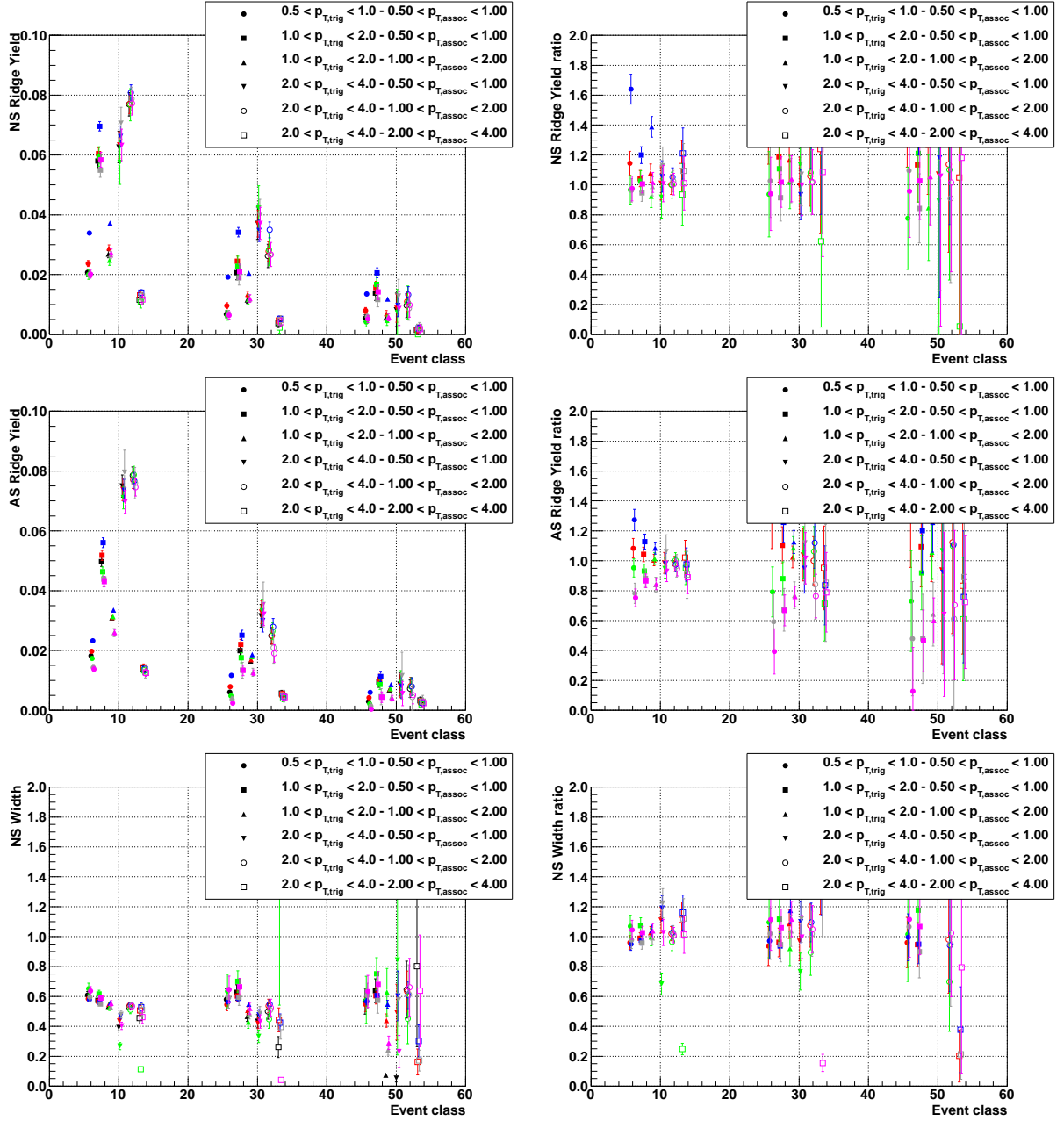


Figure 19: Systematic uncertainties evaluation. Shown are: default (black), exclusion region changed to  $|\Delta\eta| < 0.5$  (red, not used for the final uncertainties), exclusion region changed to  $|\Delta\eta| < 1.2$  (green), no exclusion region (blue, not used for the final uncertainties), removing NS excess also from AS (grey) and scaling the low multiplicity class (pink). Left panels show the effect on an observable; the right panels show the ratio to the default.

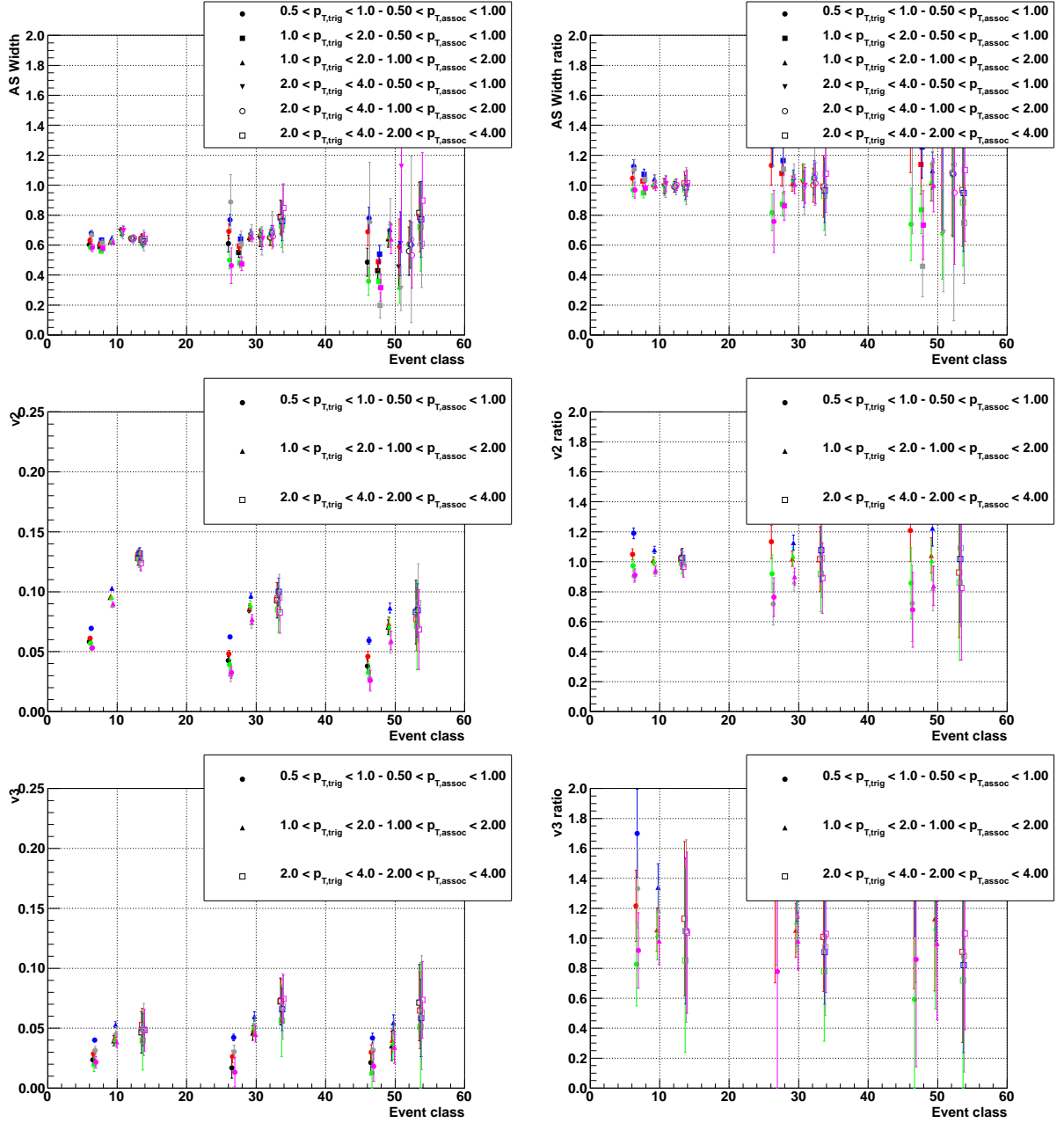


Figure 20: Systematic uncertainties evaluation. Shown are: default (black), exclusion region changed to  $|\Delta\eta| < 0.5$  (red, not used for the final uncertainties), exclusion region changed to  $|\Delta\eta| < 1.2$  (green), no exclusion region (blue, not used for the final uncertainties), removing NS excess also from AS (grey) and scaling the low multiplicity class (pink). Left panels show the effect on an observable; the right panels show the ratio to the default.

## 12.6 Summary

	$v_2$		$v_3$	
	0–20%	20–60%	0–20%	20–60%
Track cuts	2.5%		5%	
MC Generator	10%			
NS Exclusion	10%	20%	20%	40%

	NS Yield			
	0–20%		20–60%	
	$0.5 < p_{T,\text{assoc}} < 1$	other $p_T$ bins	$0.5 < p_{T,\text{assoc}} < 1$	other $p_T$ bins
	$0.5 < p_{T,\text{trig}} < 1$		$0.5 < p_{T,\text{trig}} < 1$	
Track cuts	5%			
MC Generator	5%			
Baseline	10%			
NS Exclusion	20%	10%	40%	20%

	AS Yield			
	0–20%		20–60%	
	$0.5 < p_{T,\text{assoc}} < 1$	other $p_T$ bins	$0.5 < p_{T,\text{assoc}} < 1$	other $p_T$ bins
	$0.5 < p_{T,\text{trig}} < 1$		$0.5 < p_{T,\text{trig}} < 1$	
Track cuts	5%			
MC Generator	10%			
Baseline	10%			
NS Exclusion	20%	10%	40%	20%

	NS Width		AS Width	
	0–20%	20–60%	0–20%	20–60%
Track cuts	2.5%			
MC Generator	2.5%			
Baseline	10%			
NS Exclusion	10%	20%	10%	20%

### 13 Mirroring Procedure

Projecting the two-dimensional per-trigger yields to  $\Delta\varphi$  results in Fig. 21. For this figure the systematic sources above were also evaluated; the uncertainty was found to be smaller than 0.01 (absolute) per bin.

A similar figure can be produced after subtracting the near-side ridge also on the away-side. To this end the near-side ridge structure is determined in the same event class within  $1.2 < |\Delta\eta| < 1.8$ , while the ridge on the away side is constructed by mirroring this near-side structure at  $\Delta\varphi = \pi/2$ . This subtracting procedure results in Fig. 22.

The following section discusses the mathematical similarity of this method to the the method which subtracts low from high multiplicity events.

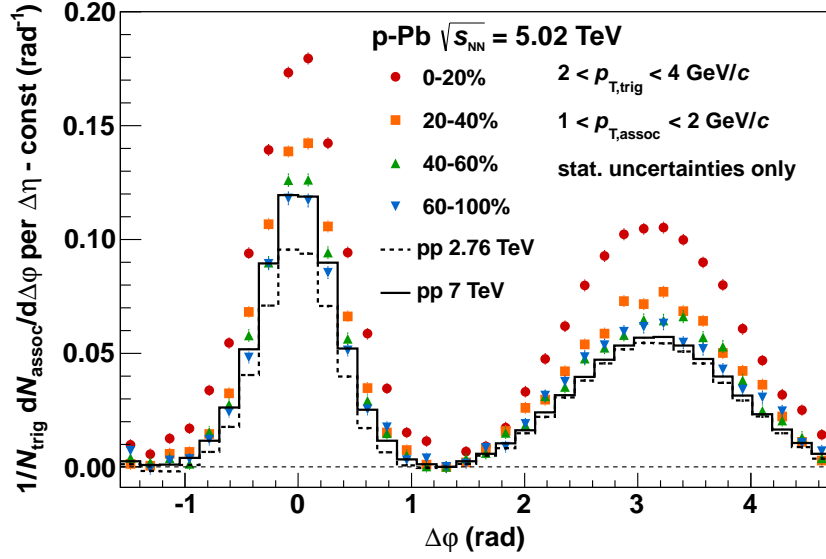


Figure 21: Associated yield per trigger particle as a function of  $\Delta\varphi$  averaged over  $|\Delta\eta| < 1.8$  for pairs of charged particles with  $2 < p_{T,\text{trig}} < 4 \text{ GeV}/c$  and  $1 < p_{T,\text{assoc}} < 2 \text{ GeV}/c$  in p-Pb collisions at  $\sqrt{s_{\text{NN}}} = 5.02 \text{ TeV}$  for different event classes, and in pp collisions at 2.76 and 7 TeV. The yield between the peaks (determined at  $\Delta\varphi \approx 1.3$ ) has been subtracted in each case. Only statistical uncertainties are shown; systematic uncertainties are less than 0.01 (absolute) per bin.

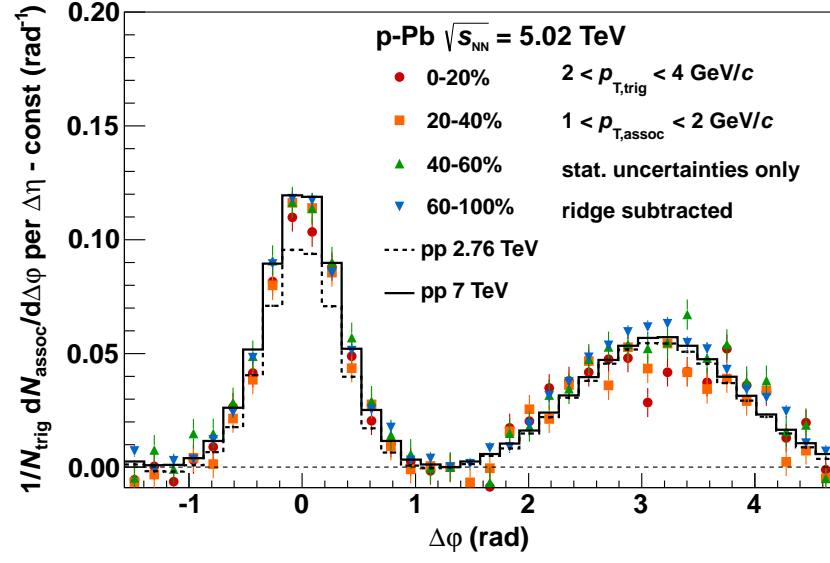


Figure 22: Same as Fig. 21 but for the event classes 0–20%, 20–40% and 40–60% the long-range contribution on the near-side  $1.2 < |\Delta\eta| < 1.8$  and  $|\Delta\varphi| < \pi/2$  has been subtracted from both the near side and the away side as described in the text.

### 13.1 Method Comparison

This section discusses the similarity of the methods proposed in Sections 8 and 13.

In the general case both near and away side have a jet  $J$  and a ridge  $R$  component

$$N_i = J_i^N + R_i^N \quad (8)$$

$$A_i = J_i^A + R_i^A \quad (9)$$

$i$  is the multiplicity class.

#### Method 1: “central - peripheral”

$$R_{1-2}^N := N_1 - N_2 = J_1^N + R_1^N - J_2^N - R_2^N \quad (10)$$

$$R_{1-2}^A := A_1 - A_2 = J_1^A + R_1^A - J_2^A - R_2^A \quad (11)$$

Experimentally we find that

$$R_{1-2}^N \approx R_{1-2}^A \quad (12)$$

Our interpretation assumes that

$$R_2^N = R_2^A = 0 \quad (13)$$

$$J_1^N = J_2^N \quad (14)$$

$$J_1^A = J_2^A \quad (15)$$

and it follows then that

$$R_1^N \approx R_1^A. \quad (16)$$

#### Method 2: “Away side - near side ridge”

$$\hat{A}_1 := A_1 - R_1^N = J_1^A + R_1^A - R_1^N \quad (17)$$

$$\hat{A}_2 := A_2 - R_2^N = J_2^A + R_2^A - R_2^N \quad (18)$$

$$\hat{N}_1 := N_1 - R_1^N = J_1^N + R_1^N - R_1^N = J_1^N \quad (19)$$

$$\hat{N}_2 := N_2 - R_2^N = J_2^N + R_2^N - R_2^N = J_2^N \quad (20)$$

Experimentally we find that

$$\hat{A}_1 \approx \hat{A}_2 \quad (21)$$

$$\hat{N}_1 \approx \hat{N}_2 \rightarrow J_1^N \approx J_2^N \quad (22)$$

Our interpretation assumes that

$$R_i^N = R_i^A \quad (23)$$



and it follows then that

$$J_1^A \approx J_2^A. \quad (24)$$

So indeed it seems that we just swap assumption and conclusion in the methods. In method1 (15) leads to (16) and in method2 (23) leads to (24).

In the following some examples are discussed under certain physics assumptions.

**Karel's idea** We can have ridges of different magnitude in a given class and still find that their *differences*  $R_{1-2}^N, R_{1-2}^A$  are the same.

We could model this in the following way:

$$R_1^N = 10R \quad (25)$$

$$R_1^A = R \quad (26)$$

$$R_2^N = 9R \quad (27)$$

$$R_2^A = 0 \quad (28)$$

Then we find experimentally in method 1, (12),

$$J_1^N + 10R - J_2^N - 9R \stackrel{?}{=} J_1^A + R - J_2^A - 0 \quad (29)$$

$$\rightarrow J_1^N - J_2^N \stackrel{?}{=} J_1^A - J_2^A \quad (30)$$

And in method 2 we find, (21),

$$J_1^A + R - 10R \stackrel{?}{=} J_2^A + 0 - 9R \quad (31)$$

$$\rightarrow J_1^A \stackrel{?}{=} J_2^A \quad (32)$$

If one finds experimentally that  $J_1^N = J_2^N$  (which we do), (30) and (32) become equivalent.

**Changes of jet yield** Let's assume that the jet yield changes from one class to the other:

$$J_1^N = J_2^N + \Delta^N \quad (33)$$

$$J_1^A = J_2^A + \Delta^A \quad (34)$$

Also here we assume only a ridge in class "1" and the same on near and away side:

$$R_1^N = R_2^A = R \quad (35)$$

$$R_2^N = R_2^A = 0 \quad (36)$$

Then we find experimentally in method 1, (12),

$$J_2^N + \Delta^N + R - J_2^N - 0 \stackrel{?}{=} J_2^A + \Delta^A + R - J_2^A - 0 \quad (37)$$

$$\rightarrow \Delta^N \stackrel{?}{=} \Delta^A \quad (38)$$

And in method 2 we find, (21),

$$J_2^A + \Delta^A + R - R \stackrel{?}{=} J_2^A + 0 - 0 \quad (39)$$

$$\rightarrow \Delta^A \stackrel{?}{=} 0 \quad (40)$$

If one finds experimentally that  $\Delta^N = 0$  (which we do), (38) and (40) become equivalent.

## References

- [1] J. F. Grosse-Oetringhaus and A. Morsch, “Jet-like peak-shapes in angular correlations in pb–pb collisions,” *ANA-56* <https://aliceinfo.cern.ch/Notes/node/33> (May, 2012) .
- [2] **ALICE** Collaboration, B. Abelev *et al.*, “Underlying event measurements in pp collisions at  $\sqrt{s} = 0.9$  and 7 TeV with the ALICE experiment at the LHC,” *JHEP* **1207** (2012) 116, [arXiv:1112.2082](#) [[hep-ex](#)].
- [3] **ALICE** Collaboration, B. Abelev *et al.*, “Pseudorapidity density of charged particles in p–Pb collisions at  $\sqrt{s_{\text{NN}}} = 5.02$  TeV,” [arXiv:1210.3615](#) [[nucl-ex](#)].
- [4] **CMS** Collaboration, S. Chatrchyan *et al.*, “Observation of long-range near-side angular correlations in proton-lead collisions at the LHC,” [arXiv:1210.5482](#) [[nucl-ex](#)].
- [5] J. L. Gramling, “Two-track resolution effects for hbt analyses in alice,” *ALICE-INT-2011-003* <https://cds.cern.ch/record/1419204> (Oct, 2011) .